SAND2021-11782J

Degradation-Resistant TiO_2@Sn Anodes for High-Capacity Lithium-Ion Batteries

Subrahmanyam Goriparti[1], Katharine L. Harrison[2], and Katherine L. Jungjohann[1*]

[1]Center for Integrated Nanotechnologies and [2] Nanoscale Sciences, Sandia National Laboratories, Albuquerque, New Mexico 87185, United States

*Corresponding author: kljungj@sandia.gov

ABSTRACT

As the demand for higher-performance batteries has increased, so has the body of research on theoretical high-capacity anode materials. However, the research has been hindered because the high-capacity anode material properties and interactions are not well understood, largely due to the difficulty of observing cycling *in situ*. Using electrochemical scanning transmission electron microscopy (ec-STEM), we report the real-time observation and electrochemical analysis of pristine tin (Sn) and titanium dioxide-coated Sn (TiO_2@Sn) electrodes during lithiation/delithiation. As expected, we observed a volume expansion of the pristine Sn electrodes during lithiation, but we further observed that the expansion was followed by Sn detachment from the current collector. Remarkably, although the TiO_2@Sn electrodes also exhibited similar volume expansion during lithiation, they showed no evidence of Sn detachment. We found that the TiO_2 surface layer acted as an electrochemically activated artificial solid-electrolyte interphase that serves to conduct Li ions. As a physical coating, it mechanically prevented Sn detachment following volume changes during cycling, providing significant degradation resistance and 80% Coulombic efficiency for a complete lithiation/delithiation cycle. Interestingly, upon delithiation,

TiO_2@Sn electrode displayed a self-healing mechanism of small pore formation in the Sn particle followed by agglomeration into several larger pores as delithiation continued.

KEYWORDS: in-situ TEM, electrochemistry, lithium ion batteries, tin anode, nanoscale, pore

INTRODUCTION

The ongoing demand for portable rechargeable energy storage devices with higher storage capacity and longer battery lifetime [1-3] has inspired extensive research in innovative, high-capacity anode materials for lithium-ion batteries (LIBs). Silicon (Si, 4200 mAh/g), germanium (Ge, 1600 mAh/g), and tin (Sn, 994 mAh/g) [4-6] have been proposed as replacements for the relatively low-capacity graphite anodes (C, 372 mAh/g). However, the current challenge for all high-capacity anode materials has been to improve cyclability and capacity retention. Numerous experimental techniques have strongly indicated that each of these anode materials demonstrates rapid volume expansion during lithiation, which causes internal strain, fracturing, and first-cycle pore formation that quickly results in a brittle anode structure [5-9]. Nevertheless, the precise failure mechanisms in the liquid electrolyte are still unconfirmed due to the difficulty of characterizing solid-liquid interfaces. In-situ electrochemical scanning transmission electron microscopy (ec-STEM) studies have circumvented this problem by characterizing anode reactions using a solid electrolyte with open-cell transmission electron microscopy (TEM) [10, 11], and their results have added weight to the theory that the primary failure mechanism is volume-expansion. However, the high overpotentials that were used in those studies to drive the Li ions into the anode through the solid LiO_X electrolyte are not representative of the electrochemical kinetics involved during the actual operation of commercial liquid-electrolyte LIBs, and, therefore, their results are still inconclusive with regard to liquid electrolyte reactions [12-17]. This is especially evident in targeted

engineering the nanoscale electrode/electrolyte interfaces for advanced performance in commercial liquid-electrolyte LIBs. Breakthroughs in truly cyclable high-capacity anodes must be guided by *operando* characterization.

Of the three high-energy alloy anode materials, Sn has the most significant effective interstitial space and most pliable matrix in addition to high electrical conductivity, which makes it the most promising practical alternative to graphite [4-8] and therefore a priority in the study of anode failure mechanisms. This work was divided into two stages. First, we used in-situ ec-STEM to characterize the solid-liquid interface of Sn with a commercially available organic-liquid electrolyte during lithiation and delithiation, as previous in-situ characterization at this scale was confined to solid-state electrolyte reactions. We found that Sn delamination from the current collector during lithiation was the primary failure mechanism for Sn as a LIB anode.

Previous studies have found that a compatible surface layer on the Sn and other alloys based anodes can create an artificial solid electrolyte interphase (SEI) barrier, inhibiting parasitic reactions between Sn and the electrolyte, [18-20]. Titanium dioxide (TiO_2) was chosen as an optimal surface layer for four primary reasons: 1.) lithiated TiO_2 (Li_xTiO_2) is ionically conductive [21], 2.) the high Li-insertion potential of TiO_2 can create an artificial SEI prior to the electrolyte reduction potential of < 1.0 V *vs* Li [22, 23], preventing loss of electrolyte to the SEI, 3.) TiO_2 has high Li-ion insertion and extraction potentials (close to 1.5 V *vs* Li) that do not overlap with the electrochemical profile of Sn (< 0.8 V *vs* Li) [24-27], and 4.) the low volume-expansion of TiO_2 upon Li insertion (< 4%) seemed unlikely to impact Sn volume changes (≈ 259%) during electrochemical cycling [6, 28, 29]. Consequently, for the second part of this project, we applied a 3 nm surface layer of amorphous TiO_2 on the Sn electrode surface (TiO_2@Sn), and then observed a complete lithiation and delithiation cycle. During delithiation of the TiO_2@Sn, in the Sn we

observed a self-healing mechanism of pore formation followed by structural reconfiguration for pore agglomeration as delithiation progressed.

EXPERIMENTAL SECTION

Ec-STEM Platform: For our in-situ experiments, we employed the custom-designed ec-STEM platforms designed by the Center for Integrated Nanotechnologies, as per the fabrication, assembly and electrochemical STEM analysis procedures outlined in previous publications [12, 15, 18, 30]. In detail, a liquid cell was constructed using two 3 × 5 mm silicon chips; the bottom chip was patterned with 10 individual tungsten (W) leads, where one end of the W lead overhangs a SiN_x window within a rectangular liquid-barrier seal ring and two alignment etched orifices. The top chip acts as a lid, with a similar SiN_x window and alignment orifices, as well as two additional electrolyte-filling ports. The W leads were buried with electrically insulative SiO_2 except for the region of the SiN_x and the bond pads.

The design and fabrication of ec-STEM liquid cells involves a multi-step process, starting with e-beam evaporation and deposition of gold on 10 bond pads connected to the W leads. The entire bottom chip was covered with a passivating layer of ~33 nm alumina (Al_2O_2, via atomic layer deposition, ALD) and ~7 nm of silica (SiO_2, through radio frequency magnetron sputtering), except over the gold bond pads. The working titanium (Ti)/Sn electrode (5/50 nm), and the counter/reference Ti electrode (50 nm) were patterned onto the bottom chip through electron-beam lithography, using a hydrofluoric acid etching of Al_2O_3/SiO_2 layer to open the electrical connection to the underlying W leads, followed by electrode material deposition using electron-beam evaporation. Finally, 3 nm of amorphous TiO_2 was deposited on the surface of the Ti/Sn working

electrode by ALD at 90°C. This customization controlled the electrochemistry such that only the desired patterned electrodes were exposed to the liquid electrolyte, and the rest of the surface was covered with a non-reactive layer of Al_2O_3/SiO_2. As a result, we were able to correlate quantitative electrochemical analysis from the working electrodes to the nanoscale imaging using bright-field STEM.

Once electrodes were patterned on the bottom chip, the top and bottom chips were perfectly aligned with ruby beads, sealed immediately with Loctite Hysol 1C-LV epoxy, and then dried for two hours at 60º C in air. The sealed cell was left to cool down to room temperature, and then affixed to a sample carrier with carbon tape, followed by wire bonding between gold bond pads (connected to W leads) on the platform with the carrier's bond pads. The wire-bonded platform carrier was transferred to a helium-filled glovebox and filled with 1M lithium hexafluoro phosphate ($LiPF_6$) in a 50:50 by volume ethylene carbonate/diethyl carbonate (EC:DEC) electrolyte under a visible-light microscope using a syringe fitted with a capillary tube. Then, both the fill ports in the lid were covered with Kapton tape and sealed with epoxy (3 M Scotch-Weld DP-100). The sealed chips were left to cure at room temperature in the glovebox for 30 - 45 minutes.

Ec-STEM Experiments: The sealed, electrolyte-filled liquid cell was inserted into a 16-lead TEM holder (Nano factory Instruments AB) with all leads connected to a custom-designed breakout box for potential grounding. All leads were connected as floating before performing the in-situ ec-STEM experiments. The electrochemical galvanostatic constant current of 0.57 $\mu A/cm^2$ charge-discharge measurements were taken using a Modulab ECS potentiostat (Ametek, Inc.) in a three-electrode format. Ti electrodes were used as a counter/reference and Sn or TiO_2@Sn as a working electrode. Simultaneously, S/TEM images were being collected from FEI Tecnai F30 S/TEM

operated at 300 kV in STEM mode. Low-beam currents of <10 pA was generally used with images acquired at 5 μs dwell times for 1k × 1k images. Electron energy loss spectroscopy using a Gatan Tridiem 863 GIF was used to determine the approximate electrolyte thickness in the region of the working electrodes on the SiN_x windows; electrolyte thickness was typically on the order of a few hundred nanometers. To achieve low-current control, a femtoammeter card was used along with a custom-built preamplifier to reduce the current going through the reference electrode below 10 fA.

Coin Cell Experiments: Coin cells were fabricated in an argon-filled glovebox using Ti/Sn (10/100 nm) or Ti/Sn/TiO_2 (10/100/3 nm) deposited on 15 μm copper foil as mentioned above by electron beam evaporation and ALD. The Sn on Cu foil was used as a working electrode against Li (750 μm, Sigma-Aldrich) foil, as the counter and reference electrodes, respectively. 1M $LIPF_6$ in EC:DEC (<5 ppm of H_2O) and Celgard 2400 were used as electrolyte and separator, respectively. All cells were rested for ∼12 h before electrochemical cycling. The cyclic voltammetry and constant current charge-discharge cycle measurements were collected with a BCS-105 Biologic instrument (Biologic Instruments, France).

Elemental Characterization. Scanning electron microscopy imaging was performed on a FEI Nova NanoLab 600 SEM. High angle annular dark-field STEM imaging and energy dispersive X-ray spectrometry analysis was performed using a 200 kV FEI ChemiSTEM, installed with an aberration-corrector and four silicon-drift detectors.

RESULTS AND DISCUSSION

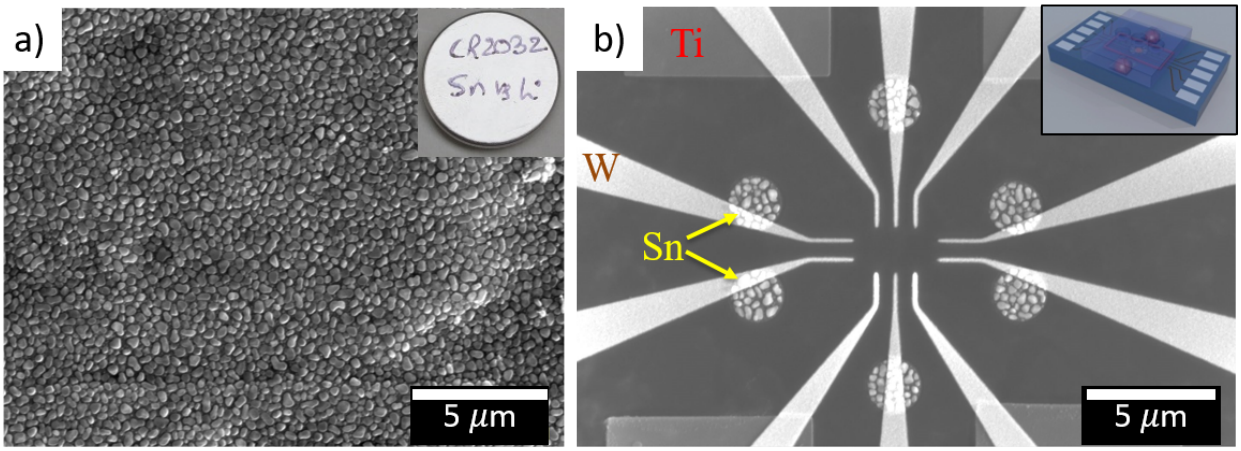

Figure 1. Scanning electron microscope images of: (a) TiO_2@Sn nanostructure anode on a copper foil for coin cell testing (*inset photograph of coin cell*); b) TiO_2@Sn anode as working electrode and Ti counter and reference electrodes on a custom-designed electrochemical liquid-cell TEM platform with passivated tungsten (W) electrical leads for ec-STEM experiments (*inset schematic of a liquid cell[30]*).

Figure 1 shows the SEM images of electron-beam-evaporated Ti/Sn films with ALD coated TiO_2 over the Cu foil (Figure 1a) and liquid cell bottom chip with patterned Ti electrode films (Figure 1b). The deposited Sn films have isolated nanosized particles with clear grain structure and sharp grain boundaries. These "island growth" textures are caused by a Volmer-Weber mechanism for deposition with coalesce into individual isolated islands to minimize the surface free energy [31, 32]. In order to provide continuous and improved electrical contact of the isolated nanosized Sn particles, 5 or 10 nm of Ti was deposited underneath the Sn nanostructures as an adhesion layer and current collector. The final TiO_2@Sn electrode films were obtained by coating the Sn film with 3 nm of TiO_2 using ALD (Figure S1).

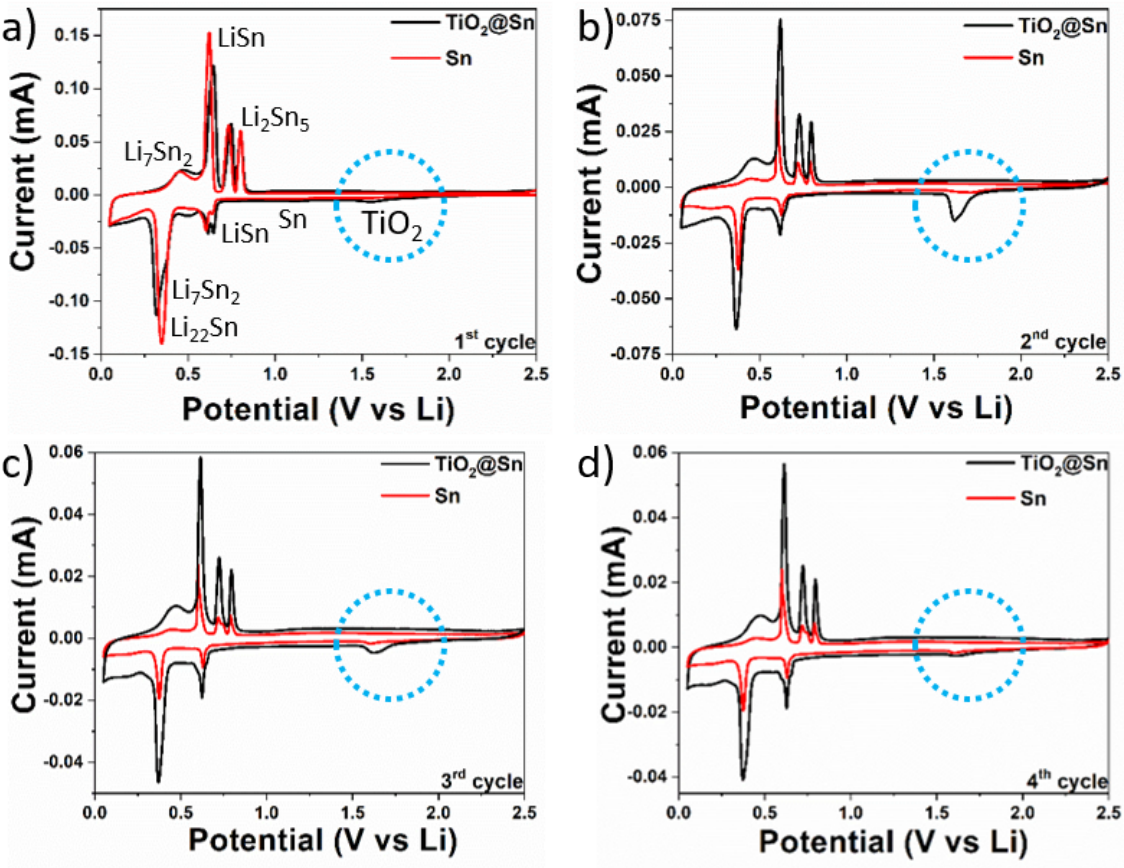

Figure 2. Cyclic voltammograms of pristine Sn and TiO_2@Sn electrodes *vs* Li at a scan rate of 0.1 mV/s and labeled for the electrochemical multi-step process of Sn lithiation/delithiation for the (a) first cycle, (b) second cycle, (c) third cycle, and (d) fourth cycle.

Coin cell analysis was used for bulk comparison of the pristine Sn and TiO_2@Sn electrodes. The electrode performance was evaluated by cycling at a constant current of 5.7 uA/cm^2 (Figure S2a-b) and cyclic voltammetry (CV) between potentials of 2.5–0.05 V *vs* Li, at a scan rate of 0.1 mV/s (Figure 2). The CVs of the TiO_2@Sn electrodes show a slight TiO_2 lithiation peak in the first cycle (Figure 2a), a dramatic peak in the second (Figure 2b), a moderate peak in the third (Figure 2c), and an almost insignificant peak in the fourth cycle (Figure 2d). Our inference is that it took several cycles for the artificial SEI to form a Li_xTiO_2 phase, as evidenced by the lack of delithiation peaks corresponding to the TiO_2 in all ten cycles. These findings were also supported by galvanostatic

lithiation and delithiation studies (Figure S2a-b). However, this bulk electrochemical comparison of the Sn anodes with and without the surface layer demonstrates the enhanced electrochemical performance of TiO_2@Sn without fully clarifying the electrochemically activated artificial SEI's role and the primary failure mechanism of the pristine Sn anodes. To compensate for this lack, we used nanoscale observation via ec-STEM.

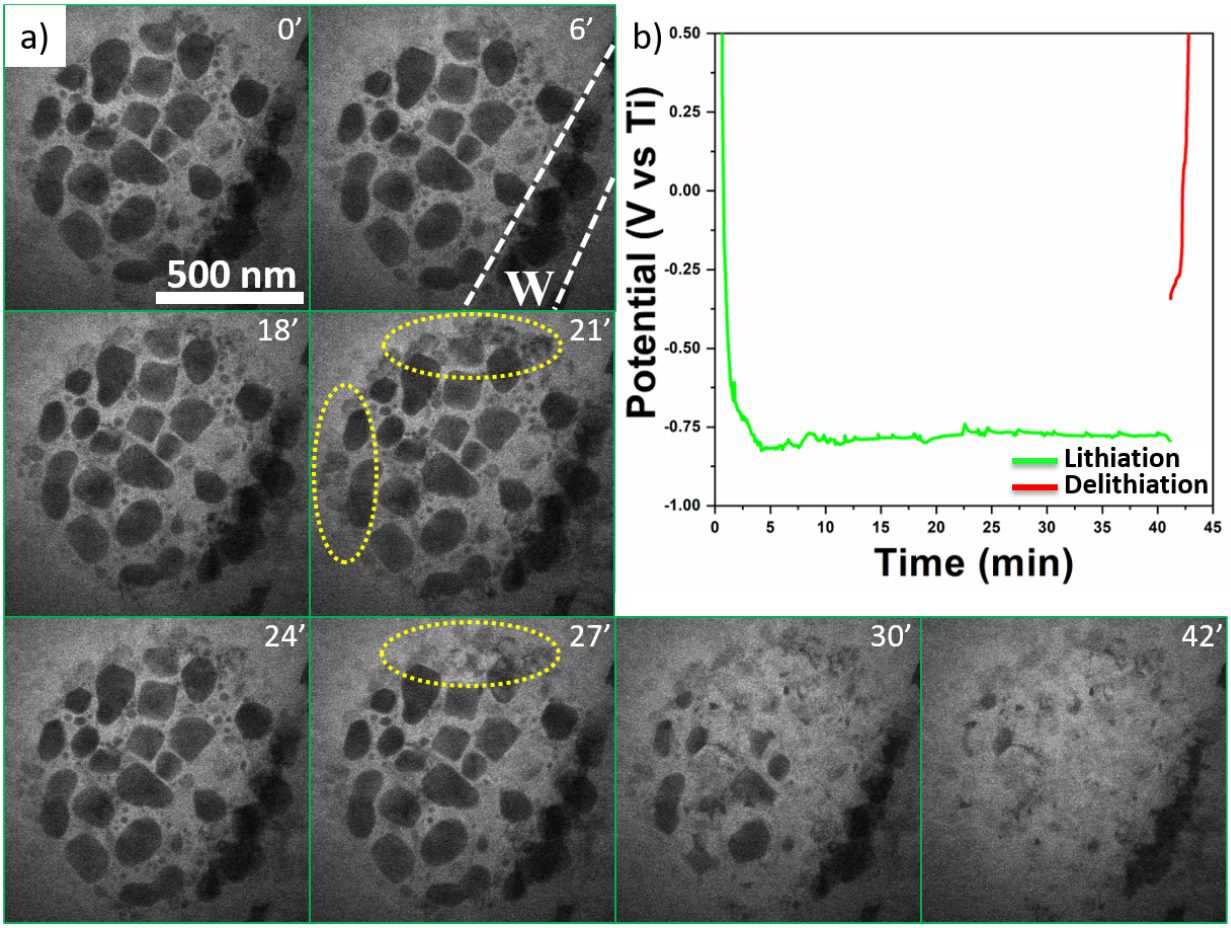

Figure 3. Bright-field ec-STEM images of (a) electrochemical lithiation of a Sn electrode at a current density of 1 mA/cm^2 (*the top right of each image represents the time since the start of the galvanostatic hold)*, where the dramatic contrast changes in the Sn grains are highlighted by the yellow dotted regions and the passivated W electrical lead can be seen in the white dotted region, and (b) the corresponding galvanostatic lithiation and delithiation profiles.

The in-situ ec-STEM investigation of the pristine Sn electrode was performed at a current density of 1 mA/cm^2 in 1 M $LiPF_6$ in EC/DEC electrolyte. During the initial lithiation, bright-field ec-STEM images revealed that the pristine Sn grains in the electrode readily delaminated from the Ti current collector after minimal volume change (Figure 3a). Slight contrast changes were observed during the first 27 minutes of lithiation, with many of the changes occurring around the perimeter of the electrode. At 30 minutes, most of the individual Sn grains were lost from the Ti current collector, although the electrochemical voltage profile did not indicate significant degradation in the electrode (Figure 3b). At 42 minutes, the electrochemical lithiation of the Sn electrode was stopped due to the inability to maintain electrical contact between the Sn grains and the current collector. The image at 42 minutes confirms that almost all the Sn grains had delaminated. The delamination of Sn grains from the current collector was not size-dependent (Figure S3 and Movie S1-S2). These findings revealed that the Sn electrode's volume expansion by lithiation can cause significant strain at the interface between Sn grains and the current collector, which can easily cause Sn grain delamination if there is no mechanism to keep Sn in contact with the current collector. In order to achieve the high theoretical Li-ion capacity for Sn anodes with an extended cycle life, this primary failure mechanism of Sn grain delamination must be overcome.

Our integration of a surface layer for the TiO_2@Sn electrodes demonstrated a gradual change in volume during the two-phase lithiation process, with pore formation and pore agglomeration during delithiation (Figure 4). Only half of the circular 3.14 μm^2 area TiO_2@Sn grain electrode is displayed in Figure 4 (Figure S4 and Movie S3-S4 shows the full electrode).The cycling was completed under the same conditions as those for the pristine Sn electrodes during ec-STEM imaging (Figure 3). Ec-STEM images of the TiO_2@Sn electrode lithiation identified darkened contrast and volume changes over time (Figure 4a). The first reaction can be seen in the

electrochemical voltage profile at -1.7 V *vs* the Ti counter electrode (Figure 4b). As previous studies using open-cell electrochemical TEM indicate, the voltage profile for the two-step lithiation observed phase transformations from Sn to Li_2Sn_5 at -1.7 V, and the crystalline-crystalline phase transformation to Li_xSn_y occurs at -3.1 V [11]. The plateau for TiO_2 lithiation is not defined due to the high ec-STEM platform impendence and the thin 3 nm film [33-35]. We perceived that indication of the TiO_2 coating during lithiation was evidenced by the first voltage plateau shift from -0.85 V in the pristine Sn anode to -1.7 V in the TiO_2@Sn anode, due to additional impedance caused by the TiO_2 and/or lithiated TiO_2 [36, 37]. The lack of an ec-STEM voltage plateau from the TiO_2 lithiation during the first cycle is consistent with the minor peak in cyclic voltammogram obtained from the bulk coin cell cycling (Figure 2c).

After the TiO_2 film lithiation was initiated, the internal Sn electrode lithiation was evaluated as an increase in the Sn grain's perimeter. We acknowledge that the bright-field STEM images do not capture z-axial structural changes beyond contrast changes that indicate increases in thickness or density, but the contrast differences are not quantifiable here. We estimate the volume changes of the TiO_2@Sn electrode by the area, which increased by 13.7% after 96 minutes of lithiation (which translates to a 21.2% volume increase, assuming a hemispherical shape of the electrode, see Figure S5 and supporting information for calculations). The lithiation image series in Figure 4a gives no evidence of cracking or fracture in the Li_xSn_y structure, although the grain grew to over 500 nm in diameter. Stress-induced fracture has been previously observed for micron-sized Sn grains undergoing lithiation [10], therefore here, the TiO_2 coating may be playing an additional role in impacting the internal stress experienced by the Sn structure during lithiation. The in-situ images up to 96 minutes shown in Figure 4a exhibit a minimal volume change, which indicated that lithiation ended at below 10% of the theoretical storage capacity for Li in Sn (259%) [6, 8]. Hence,

the Sn volume expansion may have been constrained by the coating TiO_2 film, preventing full lithiation. Lithiation was experimentally stopped when structural changes were no longer visible, although the alloying could have continued in the out-of-plane imaging direction. The incomplete lithiation of the TiO_2@Sn electrode upon the first cycle is supported by the comparison in lithiation capacity in the bulk coin cell data between the pristine Sn and TiO_2@Sn electrodes, where pristine Sn delivered higher capacity than TiO_2@Sn electrodes (Figure 2a-b).

Our two-step delithiation of the TiO_2@Sn electrode documented a previously unobserved process of pore formation and pore agglomeration, where the electrode maintained a Coulombic efficiency of 80%. Bright-field ec-STEM images during delithiation show the nucleation of many pores in the lithiated Sn grain, followed by individual pore growth, then pore agglomeration. Pores formed when the kinetics of Li-ion migration significantly exceeded those for Sn self-diffusion [38, 39]. Similar pore formation has been reported for Ge[40] and Si [41-43] anodes from in-situ open-cell ec-TEM studies under vacuum, where LiO_x has been used as a solid electrolyte. Li-ion migration energy barrier in Sn (0.39 eV) is much lower than that for Ge (0.44 eV) and Si (0.62 eV)[8], which indicates that Li atoms can easily move around in the Sn lattice. As Li diffusion is typically much faster than vacancy migration in Sn, it was unsurprising that pores evolved in the Sn grain during delithiation. Alternatively, the pores may also result from vacancies in the Sn lattice due to the formation of a stable electrochemically activated SEI from the lithiated TiO_2, which allowed passage for Li ions but not Sn ions. In this case, the increased contrast of the Sn grain density would be due to Sn self-diffusion in the lattice after Li-ion extraction (Figure 4c) [40-42]. This data suggests that the TiO_2@Sn electrodes are able to lithiate and delithiate controllably without cracking, fracturing [10], or delaminating from the current collector.

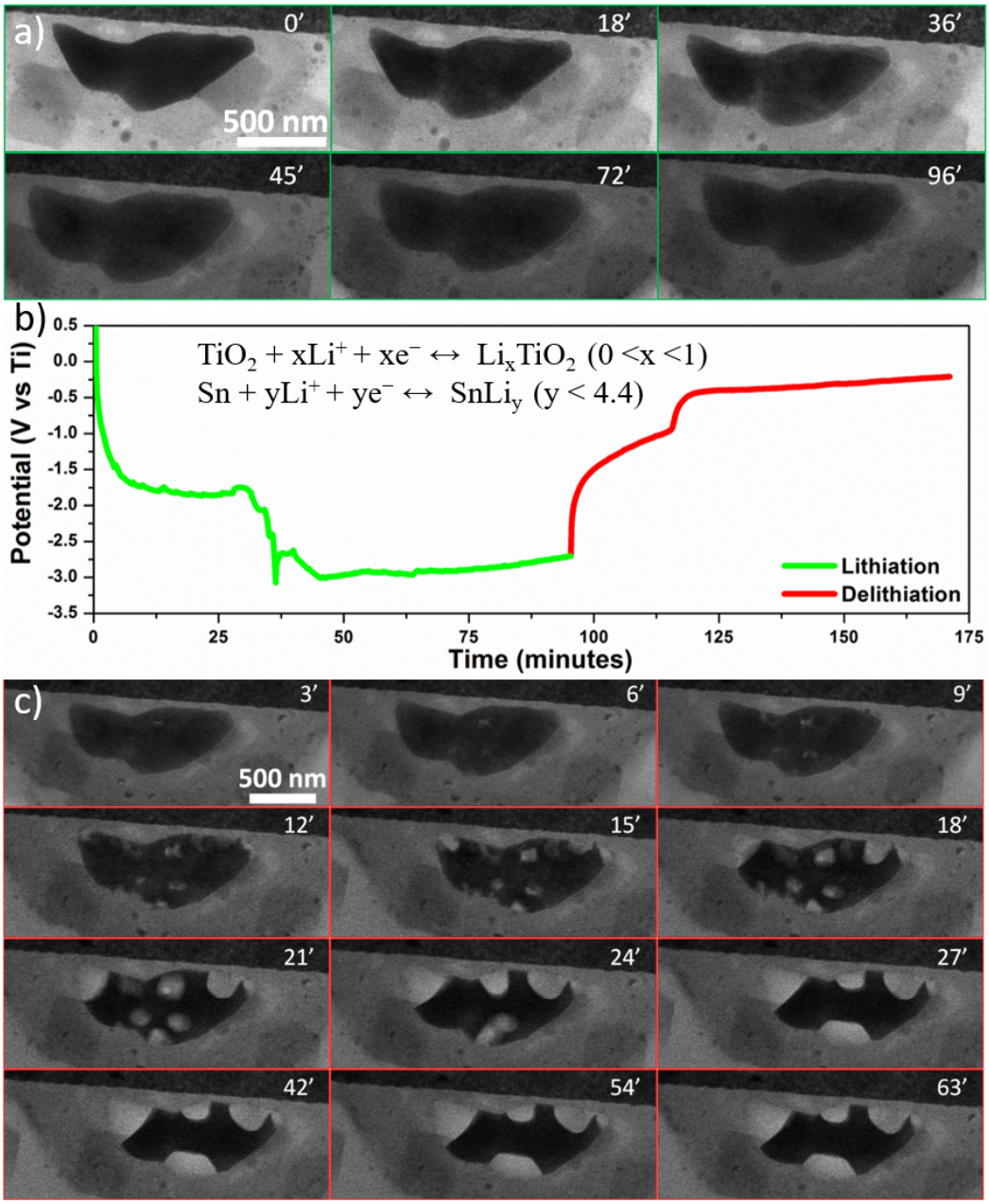

Figure 4. Bright-field ec-STEM images of the TiO_2@Sn electrode: (a) electrochemical lithiation, (b) corresponding galvanostatic lithiation and delithiation profiles at a current density of 1 mA/cm^2, and (c) electrochemical delithiation (*the top right of each image represents the time passed since the initial galvanostatic hold*).

Through qualitative comparison of the in-situ ec-STEM to the bulk coin cell electrochemical data, we can comprehensively summarize the key morphological changes that occurred in the TiO_2@Sn electrodes during one complete lithiation and delithiation cycle (Figure 4). At first, the surface layer of TiO_2 reacted with the electrolyte at 1.7 V *vs* Li, as evidenced in the coin cell studies, forming a lithiated-TiO_2 artificial SEI. Next, the Sn lithiation began as a multi-step process, with the Sn and Li_xSn ($x < 4.4$) phase transformations observed in the ec-STEM images with a volumetric increase (Figure 4a). The volume changes were effectively accommodated by the lithiated TiO_2 surface layer without fracture or cracking. Delithiation of the TiO_2@Sn electrodes resulted in the nucleation, growth, and agglomeration of many pores within the Sn grain (Figure 4b). In this regard, these in-situ ec-STEM observations provide direct evidence that a 3 nm thick TiO_2 surface layer on a 50 nm-thick Sn electrode compressed the Sn onto the current collector, which prevented Sn delamination upon cycling. These ec-STEM results indicate that high-capacity anodes (Si, Ge, and Sn) can benefit from the use of protective surface layers to enable improved Li-ion cycling performance and lifetime for incorporation into commercial LIBs.

CONCLUSION

In summary, we used custom ec-STEM techniques to observe the solid-liquid interface of a Sn electrode during lithiation and delithiation, with a commercially available organic liquid electrolyte. We confirmed that the volume change of the pristine Sn electrode caused delamination from the current collector, which was the primary failure mechanism during Sn lithiation. We further established that a conformal TiO_2 layer on the Sn electrode prevented Sn grain delamination from the current collector. We demonstrated the degradation resistance of TiO_2@Sn electrodes by obtaining 80% Coulombic efficiency in the first cycle. And we further discovered a mechanism of pore formation and pore agglomeration in the Sn grain during delithiation. This

delithiation mechanism in the TiO_2@Sn electrode is a self-healing mechanism for reducing pore formation, as pores in the electrode are a known to cause embrittlement and capacity loss over many cycles. These TiO_2@Sn electrodes demonstrate a pathway for incorporation of high-capacity anodes into commercial LIBs.

ASSOCIATED CONTENT

Supporting Information

Figure S1-S5: HAADF images, EDS mapping of TiO_2@Sn electrode, Coulombic efficiency vs cycle number of pristine Sn and TiO_2@Sn electrodes, additional replicate experiments, and estimate of volume changes after lithiation of TiO_2@Sn electrode.

Supporting Movie S1: Full pristine Sn electrode lithiation with grain size about 50-100 nm at current 1 mA/cm^2

Supporting Movie S2: Full pristine Sn electrode lithiation with grain size about 500 nm-1 μm at current 1 mA/cm^2

Supporting Movie S3: Full TiO_2@Sn electrode lithiation grain size about 500 nm-1 μm at current 1 mA/cm^2

Supporting Movie S4: Full TiO_2@Sn electrode delithiation grain size about 500 nm-1 μm at current 1 mA/cm^2

Financial Interest Statements

The authors declare no competing financial interest.

AUTHOR INFORMATION

Corresponding Author

Katherine L Jungjohann - Center for Integrated Nanotechnologies, Sandia National Laboratories, Albuquerque, NM, 87185, USA

Email: kljungj@sandia.gov

Authors

Subrahmanyam Goriparti - Centre for Integrated Nanotechnologies, Sandia National Laboratories, Albuquerque, NM, 87185, USA

Katharine Lee Harrison - Nanoscale Sciences Department, Sandia National Laboratories, Albuquerque, NM, 87185, USA

ACKOWLEDGMENTS

The authors thank to John Cumings and Zoey Warecki at the University of Maryland for initial experimental planning. This work was supported by the Nanostructures for Electrical Energy Storage (NEES), and Energy Frontier Research Center funded by the US Department of Energy, Office of Science, Basic Energy Sciences under Award Number DESC0001160 and the Laboratory Directed Research and Development program at Sandia National Laboratories. This work was performed at the Center for Integrated Nanotechnologies, an Office of Science User Facility operated for the U.S. Department of Energy (DOE) Office of Science. Sandia National Laboratories is a multimission laboratory managed and operated by National Technology & Engineering Solutions of Sandia, LLC, a wholly owned subsidiary of Honeywell International,

Inc., for the U.S. DOE's National Nuclear Security Administration under contract DE-NA-0003525. The views expressed in the article do not necessarily represent the views of the U.S. DOE or the United States Government.

REFERENCES

1. Schmuch R, Wagner R, Hörpel G, Placke T, Winter M: Performance and cost of materials for lithium-based rechargeable automotive batteries. *Nature Energy* 2018, 3:267-278.
2. Albertus P, Babinec S, Litzelman S, Newman A: Status and challenges in enabling the lithium metal electrode for high-energy and low-cost rechargeable batteries. *Nature Energy* 2018, 3:16-21.
3. Li M, Lu J, Chen Z, Amine K: 30 Years of Lithium-Ion Batteries. *Advanced Materials* 2018, 30:1800561.
4. Liu L, Xie F, Lyu J, Zhao T, Li T, Choi BG: Tin-based anode materials with well-designed architectures for next-generation lithium-ion batteries. *Journal of Power Sources* 2016, 321:11-35.
5. Li W, Sun X, Yu Y: Si-, Ge-, Sn-Based Anode Materials for Lithium-Ion Batteries: From Structure Design to Electrochemical Performance. *Small Methods* 2017, 1:1600037.
6. Liu D, Liu Zj, Li X, Xie W, Wang Q, Liu Q, Fu Y, He D: Group IVA Element (Si, Ge, Sn)-Based Alloying/Dealloying Anodes as Negative Electrodes for Full-Cell Lithium-Ion Batteries. *Small* 2017, 13:1702000.
7. Wachtler M, Besenhard JO, Winter M: Tin and tin-based intermetallics as new anode materials for lithium-ion cells. *Journal of Power Sources* 2001, 94:189-193.
8. Chou C-Y, Kim H, Hwang GS: A Comparative First-Principles Study of the Structure, Energetics, and Properties of Li–M (M = Si, Ge, Sn) Alloys. *The Journal of Physical Chemistry C* 2011, 115:20018-20026.
9. Goriparti S, Miele E, De Angelis F, Di Fabrizio E, Proietti Zaccaria R, Capiglia C: Review on recent progress of nanostructured anode materials for Li-ion batteries. *Journal of Power Sources* 2014, 257:421-443.
10. Wang J, Fan F, Liu Y, Jungjohann KL, Lee SW, Mao SX, Liu X, Zhu T: Structural Evolution and Pulverization of Tin Nanoparticles during Lithiation-Delithiation Cycling. *Journal of The Electrochemical Society* 2014, 161:F3019-F3024.
11. Li Q, Wang P, Feng Q, Mao M, Liu J, Mao SX, Wang H: In Situ TEM on the Reversibility of Nanosized Sn Anodes during the Electrochemical Reaction. *Chemistry of Materials* 2014, 26:4102-4108.
12. Leenheer AJ, Jungjohann KL, Zavadil KR, Harris CT: Phase Boundary Propagation in Li-Alloying Battery Electrodes Revealed by Liquid-Cell Transmission Electron Microscopy. *ACS Nano* 2016, 10:5670-5678.
13. Wu F, Yao N: Advances in sealed liquid cells for in-situ TEM electrochemial investigation of lithium-ion battery. *Nano Energy* 2015, 11:196-210.
14. Zeng Z, Liang W-I, Liao H-G, Xin HL, Chu Y-H, Zheng H: Visualization of Electrode–Electrolyte Interfaces in LiPF6/EC/DEC Electrolyte for Lithium Ion Batteries via in Situ TEM. *Nano Letters* 2014, 14:1745-1750.
15. Leenheer AJ, Jungjohann KL, Zavadil KR, Sullivan JP, Harris CT: Lithium Electrodeposition Dynamics in Aprotic Electrolyte Observed in Situ via Transmission Electron Microscopy. *ACS Nano* 2015, 9:4379-4389.

16. Gu M, Parent LR, Mehdi BL, Unocic RR, McDowell MT, Sacci RL, Xu W, Connell JG, Xu P, Abellan P, et al: Demonstration of an Electrochemical Liquid Cell for Operando Transmission Electron Microscopy Observation of the Lithiation/Delithiation Behavior of Si Nanowire Battery Anodes. *Nano Letters* 2013, 13:6106-6112.
17. Mackay DT, Janish MT, Sahaym U, Kotula PG, Jungjohann KL, Carter CB, Norton MG: Template-free electrochemical synthesis of tin nanostructures. *Journal of Materials Science* 2014, 49:1476-1483.
18. Harrison KL, Zavadil KR, Hahn NT, Meng X, Elam JW, Leenheer A, Zhang J-G, Jungjohann KL: Lithium Self-Discharge and Its Prevention: Direct Visualization through In Situ Electrochemical Scanning Transmission Electron Microscopy. *ACS Nano* 2017, 11:11194-11205.
19. Guan C, Wang X, Zhang Q, Fan Z, Zhang H, Fan HJ: Highly Stable and Reversible Lithium Storage in SnO2 Nanowires Surface Coated with a Uniform Hollow Shell by Atomic Layer Deposition. *Nano Letters* 2014, 14:4852-4858.
20. Chen J, Yang L, Zhang Z, Fang S, Hirano S-i: Mesoporous TiO2–Sn@C core–shell microspheres for Li-ion batteries. *Chemical Communications* 2013, 49:2792-2794.
21. Moitzheim S, De Gendt S, Vereecken PM: Investigation of the Li-Ion Insertion Mechanism for Amorphous and Anatase TiO2 Thin-Films. *Journal of The Electrochemical Society* 2019, 166:A1-A9.
22. Noh M, Kwon Y, Lee H, Cho J, Kim Y, Kim MG: Amorphous Carbon-Coated Tin Anode Material for Lithium Secondary Battery. *Chemistry of Materials* 2005, 17:1926-1929.
23. Hu T, Xie M, Zhong J, Sun H-t, Sun X, Scott S, George SM, Liu C-s, Lian J: Porous Fe2O3 nanorods anchored on nitrogen-doped graphenes and ultrathin Al2O3 coating by atomic layer deposition for long-lived lithium ion battery anode. *Carbon* 2014, 76:141-147.
24. Zhu G-N, Wang Y-G, Xia Y-Y: Ti-based compounds as anode materials for Li-ion batteries. *Energy & Environmental Science* 2012, 5:6652-6667.
25. Goriparti S, Miele E, Prato M, Scarpellini A, Marras S, Monaco S, Toma A, Messina GC, Alabastri A, Angelis FD, et al: Direct Synthesis of Carbon-Doped TiO2–Bronze Nanowires as Anode Materials for High Performance Lithium-Ion Batteries. *ACS Applied Materials & Interfaces* 2015, 7:25139-25146.
26. Bruce PG, Scrosati B, Tarascon J-M: Nanomaterials for Rechargeable Lithium Batteries. *Angewandte Chemie International Edition* 2008, 47:2930-2946.
27. Armstrong AR, Armstrong G, Canales J, Bruce PG: TiO2–B nanowires as negative electrodes for rechargeable lithium batteries. *Journal of Power Sources* 2005, 146:501-506.
28. Wagemaker M, Kearley GJ, van Well AA, Mutka H, Mulder FM: Multiple Li Positions inside Oxygen Octahedra in Lithiated TiO2 Anatase. *Journal of the American Chemical Society* 2003, 125:840-848.
29. Gao X, Sun X, Jiang Z, Wang Q, Gao N, Li H, Zhang H, Yu K, Su C: Introducing nanodiamond into TiO2-based anode for improving the performance of lithium-ion batteries. *New Journal of Chemistry* 2019, 43:3907-3912.
30. Leenheer AJ, Sullivan JP, Shaw MJ, Harris CT: A Sealed Liquid Cell for In Situ Transmission Electron Microscopy of Controlled Electrochemical Processes. *Journal of Microelectromechanical Systems* 2015, 24:1061-1068.
31. Elofsson V, Lü B, Magnfält D, Münger EP, Sarakinos K: Unravelling the physical mechanisms that determine microstructural evolution of ultrathin Volmer-Weber films. *Journal of Applied Physics* 2014, 116:044302.
32. Wei H, Eilers H: From silver nanoparticles to thin films: Evolution of microstructure and electrical conduction on glass substrates. *Journal of Physics and Chemistry of Solids* 2009, 70:459-465.

33. Memarzadeh Lotfabad E, Kalisvaart P, Cui K, Kohandehghan A, Kupsta M, Olsen B, Mitlin D: ALD TiO2 coated silicon nanowires for lithium ion battery anodes with enhanced cycling stability and coulombic efficiency. *Physical Chemistry Chemical Physics* 2013, 15:13646-13657.
34. Lotfabad EM, Kalisvaart P, Kohandehghan A, Cui K, Kupsta M, Farbod B, Mitlin D: Si nanotubes ALD coated with TiO2, TiN or Al2O3 as high performance lithium ion battery anodes. *Journal of Materials Chemistry A* 2014, 2:2504-2516.
35. Jeong G, Kim J-H, Kim Y-U, Kim Y-J: Multifunctional TiO2 coating for a SiO anode in Li-ion batteries. *Journal of Materials Chemistry* 2012, 22:7999-8004.
36. Shen BH, Veith GM, Tenhaeff WE: Silicon Surface Tethered Polymer as Artificial Solid Electrolyte Interface. *Scientific Reports* 2018, 8:11549.
37. Menkin S, Golodnitsky D, Peled E: Artificial solid-electrolyte interphase (SEI) for improved cycleability and safety of lithium–ion cells for EV applications. *Electrochemistry Communications* 2009, 11:1789-1791.
38. Liu P, Wang S, Li D, Li Y, Chen X-Q: Fast and Huge Anisotropic Diffusion of Cu (Ag) and Its Resistance on the Sn Self-diffusivity in Solid β–Sn. *Journal of Materials Science & Technology* 2016, 32:121-128.
39. Boas W, Fensham PJ: Rate of Self-Diffusion in Tin Crystals. *Nature* 1949, 164:1127-1128.
40. Lu X, He Y, Mao SX, Wang C-m, Korgel BA: Size Dependent Pore Formation in Germanium Nanowires Undergoing Reversible Delithiation Observed by In Situ TEM. *The Journal of Physical Chemistry C* 2016, 120:28825-28831.
41. Lu X, Bogart TD, Gu M, Wang C, Korgel BA: In Situ TEM Observations of Sn-Containing Silicon Nanowires Undergoing Reversible Pore Formation Due to Fast Lithiation/Delithiation Kinetics. *The Journal of Physical Chemistry C* 2015, 119:21889-21895.
42. Adkins ER, Jiang T, Luo L, Wang C-M, Korgel BA: In Situ Transmission Electron Microsopy of Oxide Shell-Induced Pore Formation in (De)lithiated Silicon Nanowires. *ACS Energy Letters* 2018, 3:2829-2834.
43. Shen C, Ge M, Luo L, Fang X, Liu Y, Zhang A, Rong J, Wang C, Zhou C: In Situ and Ex Situ TEM Study of Lithiation Behaviours of Porous Silicon Nanostructures. *Scientific Reports* 2016, 6:31334.

TOC

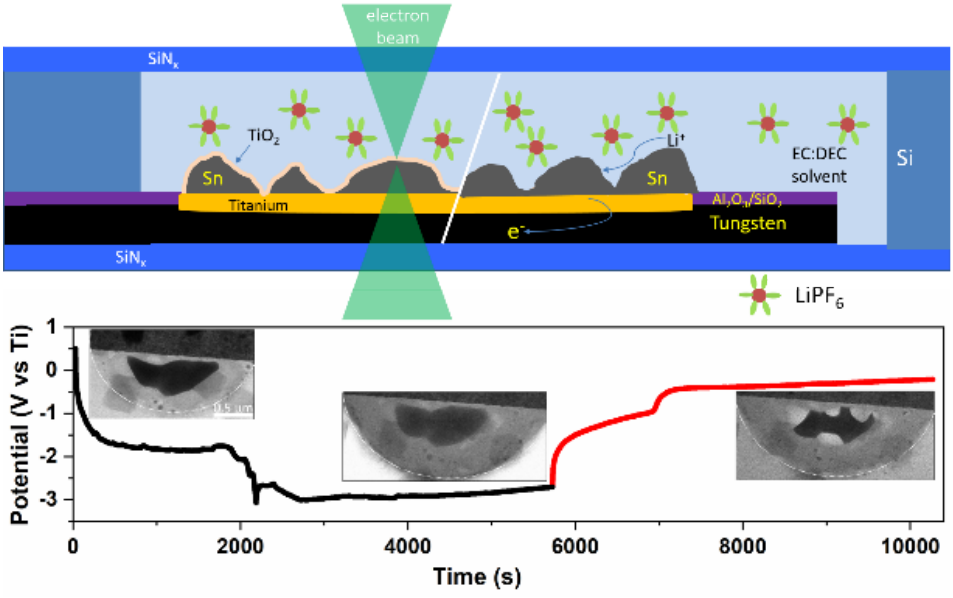
electron beam
SiNx
TiO2
Sn
Titanium
Li+
Sn
EC:DEC solvent
Si
Al2O3/SiO2
Tungsten
e-
SiNx
LiPF6
Potential (V vs Ti)
1
0
-1
-2
-3
0
2000
4000
6000
8000
10000
Time (s)